Chapter 4

Dynamic magnetic responses in dis-assemble anisotropic nanosystem

4.1 INTRODUCTION

Interacting magnetic nanosystems exhibit irrationally distinctive dynamic magnetic behaviour due to the degree and kind of interaction [1-4]. Generally, in the ensemble of interacting nanosystems, strength among constituent nanosystems, the geometrical arrangement of the ensemble and the alignment of interacting domains modulate the inherent magnetic behaviours [5-8]. However, while considering a disassembly arrangement of nanosystems, collective magnetic behaviour will get compromised and the structure correlation may affect differently the dynamic responses of domains, as compared to that of their secondary form of cluster nanosystems. The alteration in magnetic anisotropy in dis-assembly form can be achieved by adjusting size/shape/crystal structure/ compositions of MNPs [9-11]. To completely understand the magnetic behaviour in the disassembly form of nanosystems, a thorough spin dynamic investigation is essential.

Amid various morphological patterns of nanosystems, anisotropic nanorods with directional magnetic behaviour are considered as a fascinating morphology to realise the magnetic responses [16-18]. The larger aspect ratio geometry and higher magnetic moments of nanorods are found to have extraordinary inherent behaviour with potential applicability in various advanced technology fields [12-14]. The consideration of a framework comprised of anisotropic nanorods decorated with isotropic nanoparticles confers a promising platform for the understanding of physical properties dominated by quantum phenomena [14].

The occurrence of various competing energy terms in such a system shows unusual phenomena in the magnetic configurations, such as non-equilibrium spin dynamics [15, 16]. In interacting nanosystems, various quantum phenomena evolve below a certain transition temperature, for instance, slow dynamics of spins, ageing, magnetic memory effects, rejuvenation, etc. [15, 16]. Hence, the origin of such quantum phenomena in a dis-assemble arrangement of nanosystems is important to investigate through a detailed magnetic response study.

This chapter aims to provide an in-depth dynamic magnetic response study of dis-assemble anisotropic nanorods of Manganese dioxide (α-MnO_2) and isotropic nickel ferrite ($NiFe_2O_4$) hybrid nanoparticles, α-MnO_2@$NiFe_2O_4$ referred as Dis-assemble Anisotropic Nanosystem (DAN). The *ab initio* based DFT calculations are executed to check ground state magnetization. The non-equilibrium dynamics are evaluated with the aid of interacting superparamagnetic state by considering the dis-assemble morphology of anisotropic nanosystems. The structural property correlations are achieved by SAXS, SANS, XPS, etc. The existence of interacting superparamagnetic states leads to Field Cooling (FC) memory imprint below blocking temperature and wider Δt in Zero Field Cooling (ZFC) memory effect because of non-equilibrium dynamics of blocked spins. The modulated dynamic magnetic responses in dis-assemble morphology with significant magneto-crystalline anisotropy, exchange field, prominent FC/ZFC memory effects, and asymmetric ageing relaxation are explored herein.

4.2 EXPERIMENTAL DETAILS

The synthesis procedure is similar to the previous chapter [17] with a modification. All the needed precursors are acquired from Zenith, India. At first, $NiFe_2O_4$ nanoparticles are synthesised using a hydrothermal synthesis. An accurate stoichiometric amount of $FeCl_3.6H_2O$, $NiCl_2.6H_2O$, urea, and Polyvinylpyrrolidone (PVP) is dissolved in DI water. Then solution is kept in an

autoclave for 12 h at 180°C. After 12 h, the solution is left to cool to get 300 K. The achieved precipitate is centrifuged and washed. The collected sample is kept for drying for 12 h at a temperature of nearly 80°C and the nanoparticles are collected. After the development of Nickel Ferrite ($NiFe_2O_4$) nanoparticles, Manganese dioxide (α-MnO_2) is synthesised with $NiFe_2O_4$ nanoparticles through a hydrothermal synthesis procedure. A stoichiometric quantity of Potassium Permanganate ($KMnO_4$) is mixed with an appropriate quantity of deionized water and a homogeneous solution is achieved. 37 wt% hydrochloric acid (HCl) of an amount of 1.4 mL is mixed dropwise following mechanical stirring. An amount of 0.4 g of $NiFe_2O_4$ is mixed following sonication for 15 mins to get a well-dispersed mixture. The mixture is transferred to autoclave for hydrothermal reaction at 110°C for 12 h to achieve α-MnO_2 phase (in Chapter 3, 6 h hydrothermal treatment is done to achieve δ-MnO_2 phase). Then, after cooling, the precipitation is collected by centrifugation and sample is kept for drying at 60°C for 12 h after multiple washing using water and ethanol. The instrumental details are the same as mentioned in Chapter 3.

4.3 COMPUTATIONAL DETAILS

The *ab initio* Density functional theory (DFT) simulations are performed to simulate electronic behaviour of α-MnO_2@$NiFe_2O_4$ as depicted in Figure 4.4 (a). The effect of spin-polarization is considered to achieve a self-consistent ferromagnetic ground state in the considered structures. As mentioned in Chapter 3, the spin-polarized calculations are executed based on Kohn-Sham equations following plane-wave basis sets as merged in Quantum ESPRESSO software package [18]. 80 atoms are considered to perform the *ab initio* calculations for numerous determinations such as electronic property study, determination of magnetic moment, and spin-density distributions. The BFGS algorithm is used to achieve optimized crystal geometry. The system displays 744 electrons and 446 Kohn-Sham states. The electron-core corrections are implemented by considering USPP formed by RRKJ method [19]. LDA is

considered for the exchange-correlation term. [20]. Herein, a strongly-correlated interaction is considered by integrating the exchange parameter (Hubbard, U ~ 4 eV) [21]. As described in Chapter 3, Brillouin zone (BZ) sampling is maintained by anticipating a 3 x 3 x 3 unshifted Monkhorst-pack (MP) grid [22] to reach the convergence of the considered system. A 10^{-6} Ry convergence threshold accompanied by Davidson diagonalization with a cut-off energy of 40 Ry for intensifying the plane-wave basis sets. A 9 x 9 x 9 denser k-mesh grid through a tetrahedron non-self-consistent method is considered for electronic structure calculations. A k-path of Γ-X-M-Γ which is highly symmetric is considered for electronic band structure calculation.

4.4 RESULTS AND DISCUSSIONS

4.4.1 Microstructural study

For microstructural analysis of the as-synthesised system, XPS analysis is executed as provided in Figure 4.1(a-d) for elemental composition and oxidation of the system. As depicted in Figure 4.1(a), Mn 2P peaks are found at around 642.10 eV and 653.90 eV corresponding to Mn $2P_{1/2}$ and Mn $2P_{3/2}$ with an amount of 11.8 eV spin-energy separation, confirming the presence of α-MnO_2 [23]. Figure 4.1(b) shows the main peaks of Ni 2P at around 872.30 eV and 853.90 eV for Ni $2P_{1/2}$ and Ni $2P_{3/2}$ with 18.40 eV spin-energy separation [24]. A shake-up satellite peak is centred at around 859.740 eV, confirming the existence of Ni^{2+}. The detailed Fe 2P spectrum is shown in Figure 4.1 (c), which represents peaks at around 710.60 eV and 724.0 eV for Fe $2P_{1/2}$ and Fe $2P_{3/2}$ [24]. Furthermore, O 1S spectrum peaks are observed at about 529.10 eV, 529.90 eV, and 532.10 eV as shown in Figure 4.1(d). The electronic state analysis ensures the formation of α-MnO_2@$NiFe_2O_4$ [23, 24].
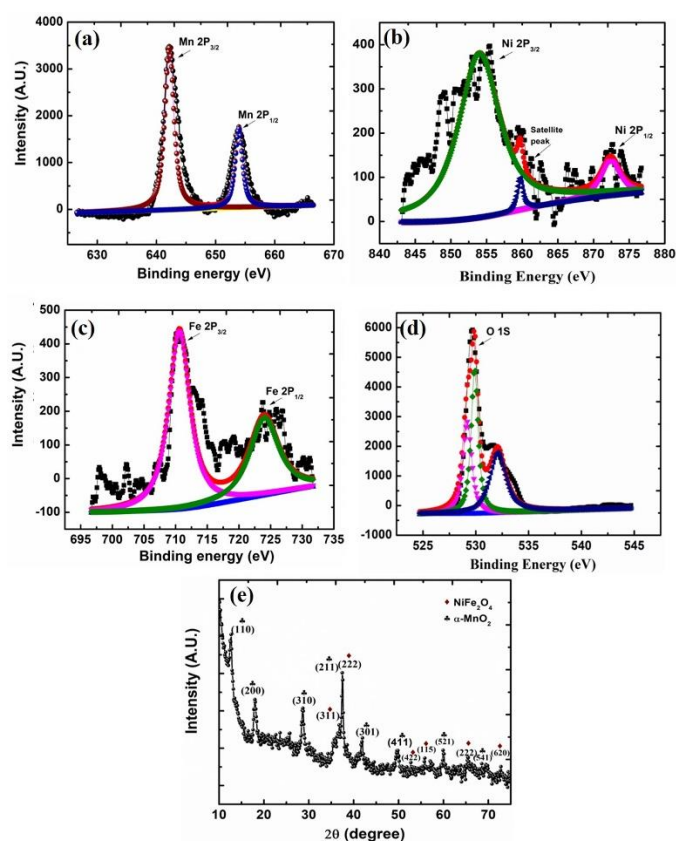
Figure 4.1: Microstructural study: XPS study (a) Mn 2P, (b) Ni 2P, (c) Fe 2P, (d) O 1s; and (e) XRD pattern of α-MnO$_2$@NiFe$_2$O$_4$.

The PXRD analysis is performed as shown in Figure 4 1(e). The obtained planes (110), (200), (310), (211), (301), (411), (521), and (541) confirm the formation of α-MnO$_2$ with JCPDS file no. 044-0141. The observed planes (311), (222), (422), (115), and (620) are confirming cubic spinel phase of NiFe$_2$O$_4$ (JCPDS Card No. 10-0325) having space group Fd-3m. Hence the pure phase of α-MnO$_2$@NiFe$_2$O$_4$ is further confirmed with the dominance of the cubic phase. However, with reaction period enhancement to 12 h, 2D flakes, as shown in Chapter 3, no longer retain their morphology and the individual flakes are curled perfectly to form a rod kind of morphology. Most of the ensembles are disintegrated in this stage and a non-uniform distribution of rod of MnO$_2$ and nickel ferrite nanoparticles are seen from FESEM images as shown in Figure 4.2(a, b). Additionally, TEM images are given in Figure 4.2(c) and Figure 4.2(d), from which the formation of rod-shaped

morphology is further evident. The bulk crystals, as observed in certain areas of Figure 4.2 (a), are due to the agglomeration of Nickel Ferrite nanoparticles, which generally occurs as a result of hydrothermal synthesis. The nanorod structure observed in the micrograph is of α-MnO$_2$.
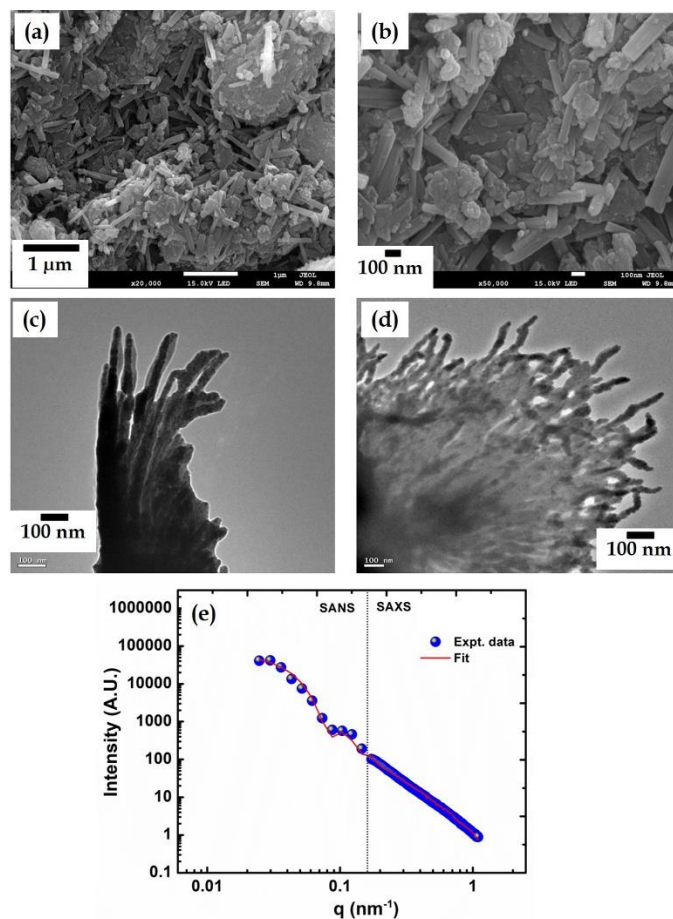

Figure 4.2: Micrographs of (a, b) FESEM, (c, d) TEM, (e) SAXS and SANS intensity profile fitting of α-MnO$_2$@NiFe$_2$O$_4$.

For structural correlation analysis, SAXS and SANS intensity profile fittings are depicted as shown in Figure 4.2(e). SAXS intensity profiles are fitted by two form factor contributions. A flat cylinder form factor with 2.8 nm radius and 8.9 nm length with 0.14 polydispersity is considered to attain information about the primary nanosystems. Another form factor contribution of the sphere model is considered with log-normal size distribution. The fitting gives a size of 10 nm and 0.6 polydispersity index. This spherical form factor contribution is arising

due to the nickel ferrite nanoparticles' contribution. SANS intensity profile is fitted by taking a spherical form factor with 52 nm radius and 0.1 polydispersity index. Though the system DAN is in disassembled form, but few contributions are coming from some broken ensembles, which are present in the system. Hence, the SAXS and SANS analyses confirm the existence of two kinds of hierarchy [25, 26].
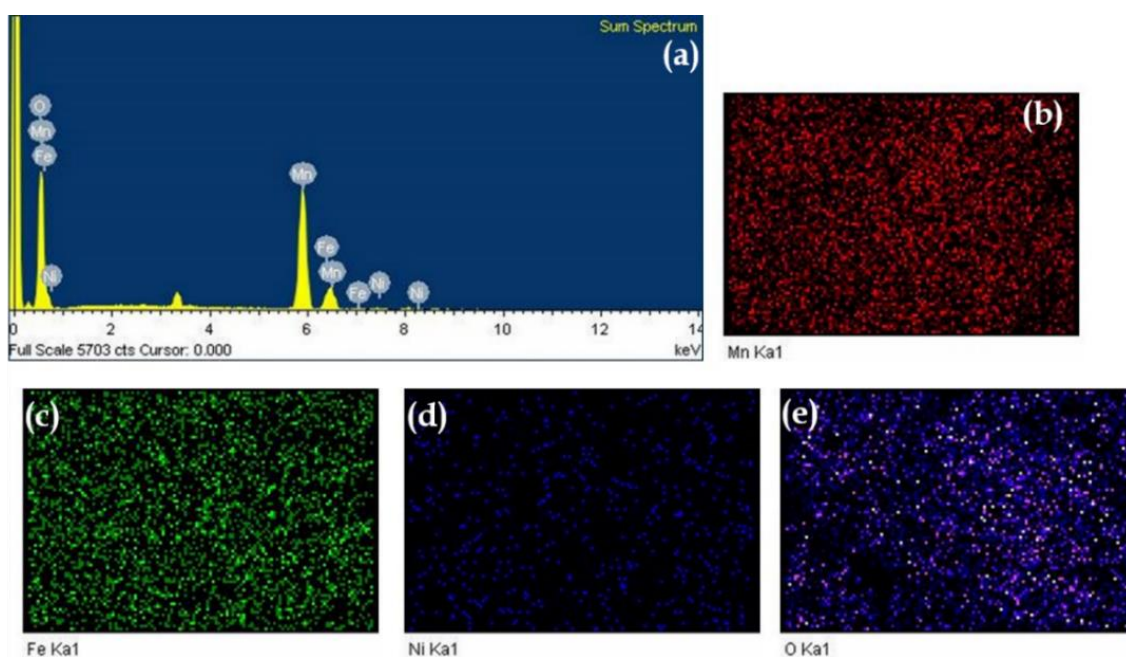

Figure 4.3: EDX microanalysis of α-MnO$_2$@NiFe$_2$O$_4$: (a) Sum spectrum of the elements, elementary mapping of (b) Mn, (c) Ni, (c) Fe, and (d) O.

To further get a confirmation of constituent elements, the elementary mapping is performed with the aid of EDX analysis as shown in Figure 4.3. The sum spectrum and all the elementary mappings confirm the Mn, O, Ni, and O elements with various atomic compositions as given in Table 4.1. The intense peak in the low energy range in the sum spectrum is due to Carbon tape.

Table 4.1 Elementary composition achieved from EDX analysis.

Element	Weight %	Atomic %
Mn	37.96	27.59
Ni	1.28	0.62
Fe	7.73	3.96
O	37.96	67.83

4.4.2 Atomic Configuration and Electronic structure

Figure 4.4 (a) displays the crystal geometry of constituent α-MnO_2@$NiFe_2O_4$. The lattice parameter is observed to be 8.48 Å. The ground state ferromagnetic structure is attained self-consistently with 46.73 μ_B/cell of total magnetization. A total Kinetic energy of -8185.7267 Ry is achieved. The electronic band structure for α-MnO_2@$NiFe_2O_4$ depicts a smooth pattern due to the lower binding site between α-MnO_2 and $NiFe_2O_4$ as shown in Figure 4.4 (b). It is observed that the system displays metallic behaviour at the Fermi energy (E_F) [27]. The observed sharp-spike like structures in density of states (DOS) (as shown in Figure 4.4 (c)) indicate existence of a ferromagnetic nature. It is manifested that ferromagnetic ordering still sustains after the incorporation of $NiFe_2O_4$ in α-MnO_2, though a variation in total magnetization is found.
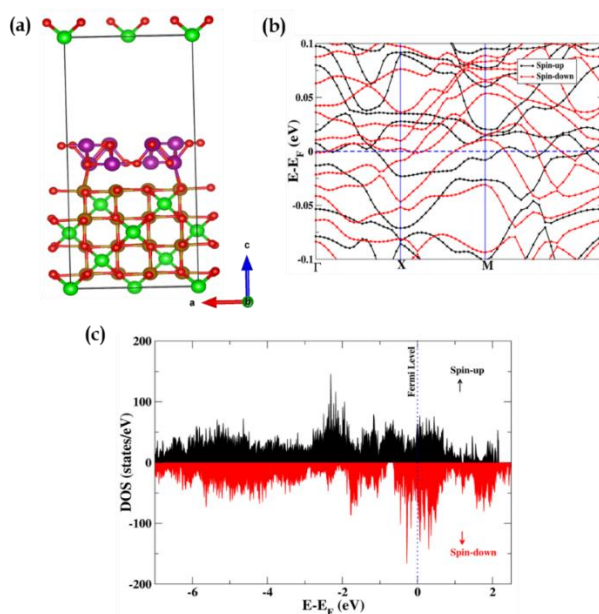
Figure 4.4: (a) Atomic configuration: the violet, green, golden, and red spheres correspond to Mn, Ni, Fe, and O, respectively, (b) Electronic band structure, and (c) determination of DOS of α-MnO$_2$@NiFe$_2$O$_4$.

Figure 4.5(a) shows spin density distribution with an iso-surface 0.0500911 e/Å^3. The yellow and blue cyan colours portray the parallel and antiparallel states. An average magnetic moment per Mn atom site in DAN is found to be -0.067 µ$_B$, which indicates that antiparallel states (cyan colour) are reflected in the Mn atom due to its lower bonding site and weaker interaction energy with NiFe$_2$O$_4$ system [27, 28]. Figure 4.5(c) shows electron density distribution mapping for the range of intensity from 0 to 1, in which red and cyan colours represent electron localization and delocalization respectively. This trend corroborates with the Figure 4.5(a). Figure 4.5(b) shows the projected density of states (PDOS), which outlines the orbital contribution of the elements of the structure such as Fe, Mn, Ni and O atoms. Figure 4.5(c) shows that the orbital contribution for Fe, Ni and O is following the same trend for both left and right panel, whereas the Mn atom site exhibits both parallel and antiparallel states. The less intense curve displays the parallel states (left) of the Mn atom site indicating the low contribution of the 4d-orbital, whereas the highly intense curve depicts antiparallel states (right),

which indicates the higher contribution of 4d-orbital of the Mn atom site. The observed reflection of PDOS (Figure 4.5(c)) validates further the spin density distribution as shown in Figure 4.5(a).
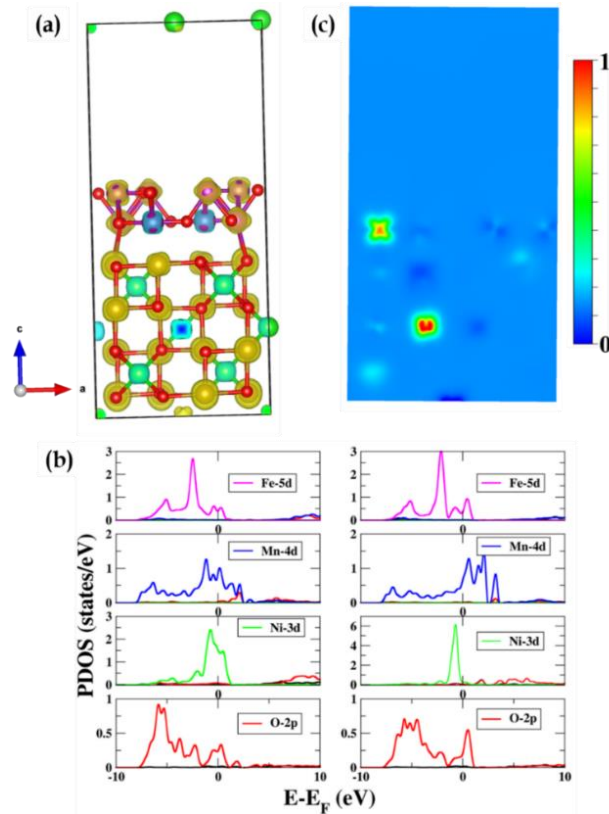

Figure 4.5: (a) Spin density distribution with an iso-surface value of 0.0529096 e/Å³, (b) Projected density of states (PDOS) individually for iron (Fe), manganese (Mn), nickel (Ni) and oxygen (O), respectively. (c) Electron density distribution with an intensity range of 0 to 1 of α-MnO_2@$NiFe_2O_4$.

4.4.3 Direct Current Magnetization study

The field-dependent magnetization analysis is executed as depicted in Figure 4.6(a, b) at 300 K, 150 K, and 5 K respectively. The observed 'S' shaped hysteresis shape ensures existence of a superparamagnetic state at room temperature [29, 30]. The coercivity (H_c) and remanence (H_r) values are calculated from the hysteresis patterns. We obtain, H_c = 16.7 Oe and H_r = 0.08 emu/g for 300 K, H_c = 20.1 Oe and H_r = 1.460 emu/g at 150 K, H_c = 212 Oe and H_r = 1.250 emu/g at 5 K

respectively. The ferromagnetism nature with higher coercivity value at low temperature is a typical signature of a superparamagnetic system. For further evaluation of magneto-crystalline anisotropy constant and saturation magnetization, LAS [31] fitting is performed using equation 2.7 of Chapter 2, for a range of 500 Oe to 15000 Oe with
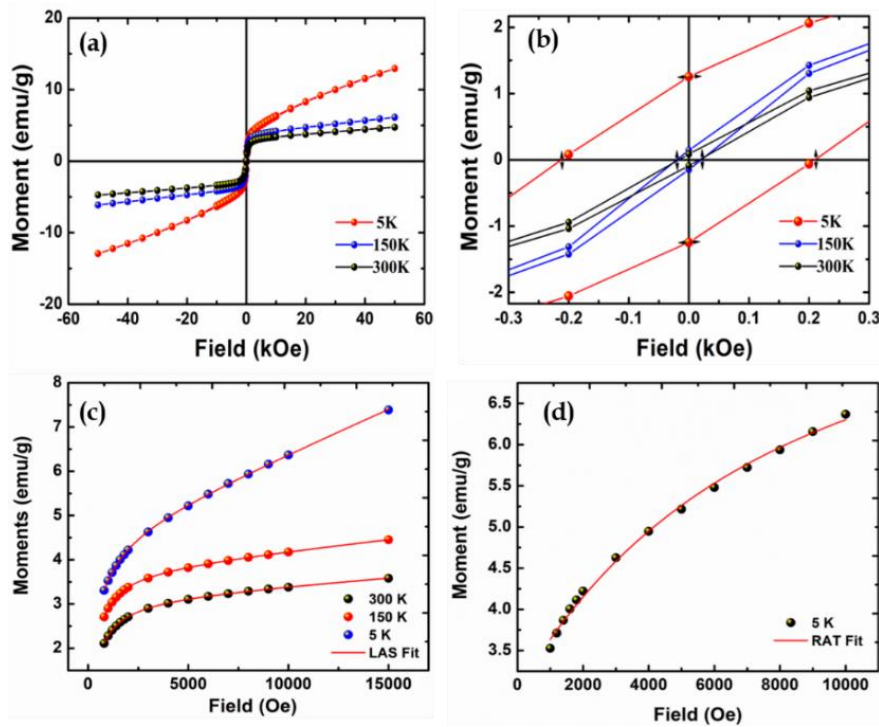

Figure 4.6: DC magnetization of α-MnO$_2$@NiFe$_2$O$_4$.**:** (a) Field-dependent magnetization study, (b) Zoomed view of hysteresis loop at different temperatures, (c) LAS fitting at 5 K, 150 K, and 300 K, (d) RAT fitting at 5 K.

all the considered temperature to achieve the trend of thermal-dependent magneto-crystalline anisotropy, as depicted in Figure 4.6(c).

For LAS fitting, 5 K, 150 K, and 300 K temperatures are considered. After proper fitting, the achieved values for M$_s$ and K are, at 5 K: M$_s$ = 4.60 emu/g and K = 5.20 × 10^3 erg/cm^3; at 150 K: M$_s$ = 3.80 emu/g and K = 3.0 × 10^3 erg/cm^3; and at 300 K: M$_s$ = 3.20 emu/g and K = 3.05 × 10^3 erg/cm^3. A significant dominance of

magnetic anisotropy is evident from the LAS investigation at low temperature for the considered dis-assemble form of the system.

Further, Random Anisotropy Theory (RAT) [32, 33, 34] is executed, using equation 3.5 of Chapter 3, for evaluation of magnetic anisotropy role in low-temperature regime by performing the fitting of field relying on magnetization as depicted in Figure 4.6(d). After proper fitting of field-dependent magnetization data considering the range of 1000 Oe to 10000 Oe at 5 K, fitted parameters are achieved as anisotropy field, H_r = 46 kOe and exchange field, H_{ex} = 14 kOe at 5 K. The higher H_r is a typical signature of the dominance of higher magnetic anisotropy and the existence of an exchange field in the interacting domains at low temperature. Henceforth, temperature-dependent magnetization behaviour is implemented to comprehend the blocking/freeing of constituent moments of the dis-assemble framework.
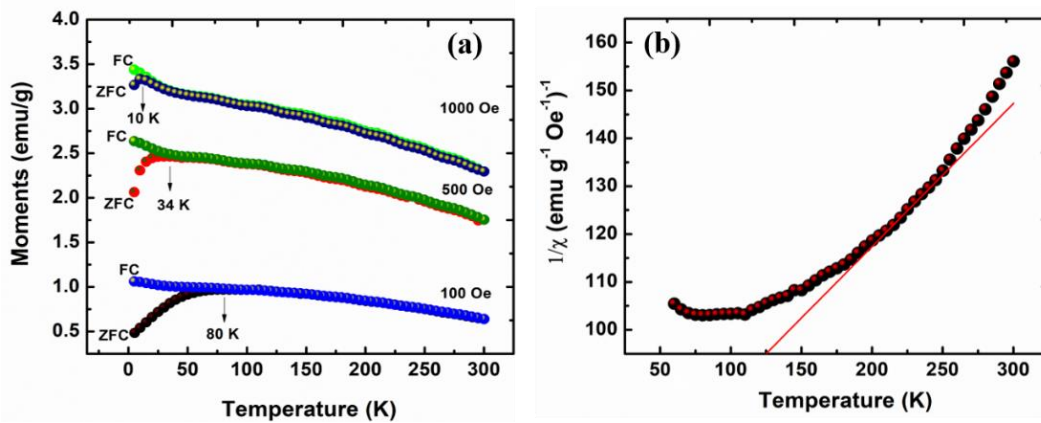

Figure 4.7: (a) Temperature-dependent magnetization study at field 1000 Oe and 100 Oe (The blocking temperature is shown with a downward arrow in both the Zero Field Cooling (ZFC) curve); (b) Curie-Weiss (CW) law fitting of α-MnO_2@$NiFe_2O_4$ and red fitting line represents CW law fitting line.

The temperature-dependent magnetization analysis is performed using two protocols: ZFC and FC for the range of 2-300 K at three magnetic fields such as 100 Oe, 500 Oe, and 1000 Oe as presented in Figure 4.7(a). The observed

divergence of ZFC and FC magnetization curves which is addressed as bifurcation is obtained at low temperature for all magnetic fields. The observed temperature cusp is found at 10 K for 1000 Oe, 34 K for 500 Oe, and nearly 80 K for 100 Oe. With increase in field, difference between moments of ZFC and FC conditions, $\Delta\chi$, is found to be decreasing, which is a typical signature of the existence of an interacting state [29, 30]. However, below blocking temperature, magnetization is observed to be increased which discards existence of SG state.

Furthermore, as depicted in Figure 4.7(b), the modified Curie-Weiss (CW) law [36] is employed, similarly the equation 3.6 of Chapter 3, by considering the inverse susceptibility, $1/\chi$ in the high-temperature region. In the CW model, χ_0 refers to thermal energy-independent susceptibility ascribed from the diamagnetic Larmor core along with Landau susceptibility and Pauli paramagnetic spin of conduction electrons. C refers Curie constant and θ_{CW} gives CW temperature. Herein, the value of θ_{CW} is achieved at around 125 K and Curie constant, C value as 3.3 cm³K mol⁻¹ is found. The effective magnetic moment, $\mu_{eff} = \sqrt{3k_B C/N_A}$ (where N_A gives the value of Avogadro's number) is found as ~ 0.9 μ_B. The positive CW temperature ensures the dominance of ferromagnetic domains in the system above curie temperature. As per mean-field theory, CW temperature is the addition of exchange couplings present in the system. For a further in-detail understanding of such interacting domains, an ac susceptibility study is performed as given in the next section.

4.4.4 AC susceptibility study

AC susceptibility is executed for evaluation of dynamic magnetic responses by considering various frequencies in 93 Hz to 9724 Hz range and temperature range of 2K-350 K. An exciting 10 Oe ac field is imposed with no dc field and frequency dependence ac susceptibility of real (χ') and imaginary (χ'') components are represented in Figure 4.8(a, b) as a function of temperature. It is seen that at a frequency of 93 Hz, a distinct anomaly is observed at around 155 K

and the peak temperature shows a frequency-dependent behaviour. As observed in Figure 4.8(a), the temperature-dependent curves execute a shifting of peak location towards higher temperature with an increase in frequency [36]. Such frequency-dependent trend is a typical signature of either the development of spin freezing or superparamagnetic blocking of spins. For further confirmation, the Mydosh parameter, k, is measured using equation 2.9 of Chapter 2. The k value is measured as ~ 0.089. In the case of SPM where there is no interaction among the nanoparticles, k gives a value between 0.1 to 0.28 [36]. Generally, for interacting systems or systems dominated by spin-glass states, the value of k ranges in an order of $10^{-2} - 10^{-3}$. The value is higher than conventional SG systems. But, lies in the range of cluster spin glass systems or interacting superparamagnetic systems [36, 37]. Therefore, further execution of spin dynamics is required to confirm whether the temperature anomaly is attributed to spin freezing or spin blocking. The presence of interacting clusters can be validated by considering Arrhenius law using equation 2.10 of Chapter 2. The fitting plot of ln(τ) with respect to T_f is shown in Figure 4.9(a) and fitting parameters give in unphysical values such as flipping period, $\tau_0 = 9.2 \times 10^{-17}$ s and activation energy, $\frac{E_a}{k_B} = 4691$ K and discard the existence of the non-interacting superparamagnetic state. Further, VF law is considered as per equation 2.11 of Chapter 2, to check magnetic interaction [36, 38]. The fitting plot of ln(τ) with T_f is shown in Figure 4.9(b) and the obtained values are: flipping period, $\tau_0 = 2.6 \times 10^{-9}$ s, activation energy, $\frac{E_a}{k_B} = 688.6$ K, and VF temperature, $T_0 = 103$ K. The non-zero value of T_0 supports existence of interaction among the domains and observed value of τ_0 further supports the
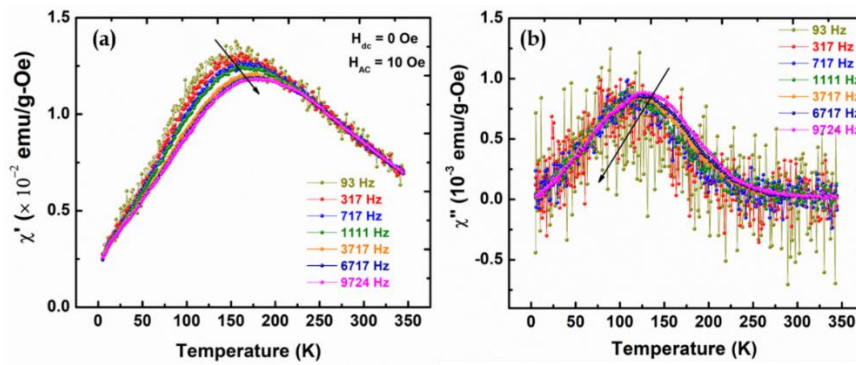
Figure 4.8: AC susceptibility (a) in phase, (b) out of phase of α-MnO$_2$@NiFe$_2$O$_4$. The arrow mark indicates the change in the peak of T$_{max}$ and χ$_{max}$ with an increase in frequency.

interacting superparamagnetic state. To examine the coupling strength among the magnetic entities, a comparison can be drawn by considering a few conditions such as for strong coupling, T$_0$ >> Ea/k$_B$ as well as T$_0$ << Ea/k$_B$ for weak coupling strength [36-41]. Herein, the system shows $\frac{E_a}{k_B}$ ~6.6 T$_0$ which resides in the intermediate range, hinting at the existence of finite interactions among the nanosystems. However, the Tholence criterion is considered as δT$_{Th}$ = $\frac{T_f - T_0}{T_f}$ to further ensure the classification of states and the value is achieved as, 0.2 which validates the formation of cluster spin-glass or interacting superparamagnetic system [36]. Hence, dynamic scaling theory is considered. In accordance with dynamic scaling theory, the power law is considered which is a primary law to examine frequency-dependence of freezing temperature [36]. To fit freezing temperature trend, the power law is considered as per equation 2.13 of Chapter 2. The plot of log(τ) vs. T$_f$ is shown in Figure 4.9 (c) and best fitting with power law gives out the values as a critical exponent, zv' = 3.4, relaxation period, τ* = 1.6 × 10^{-7} s, and glass transition temperature, T$_g$= 145 K. The parameters are crucial for classifying whether the system is dominated by spin freezing or spin blocking. The value of zv' has not come under the range of cluster glassy phase, ensuring that the system is dominated by interacting superparamagnetic phase

[36-39], which is expected from the low-temperature magnetization trend found in dc magnetization.
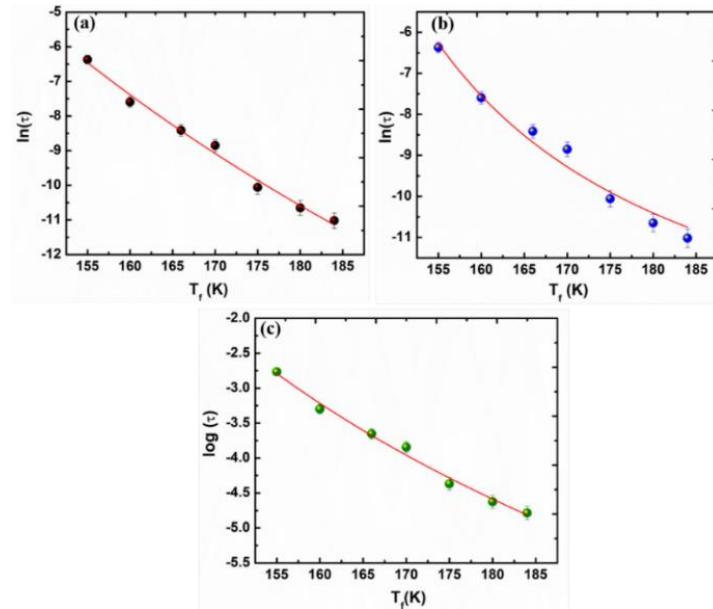

Figure 4.9: (a) Arrhenius equation fitting, (b) VF fitting, (c) Critical slowing down model fitting of α-MnO$_2$@NiFe$_2$O$_4$. (The error bars represent standard deviation in experimental data).

4.4.5 Nonequilibrium dynamics

4.4.5.1 Magnetic memory effect

To analyze low-temperature spin dynamics, magnetic memory effects [40, 41] are performed considering both the ZFC and FC protocols similar to Chapter 3 and the memory imprints are shown in Figure 4.10. For FC protocol, the system is left for cooling in 100 Oe field from room temperature to the lowest possible temperature with halting temperatures, T$_{stop}$ = 20 K, 40 K, 60 K, and 80 K of halting duration 1 h each and the moment is recorded. At each halting temperature, field is off following the lapse of waiting period, the very same magnetic field is restored following the re-cooling of the system. The recorded magnetization in this step is recorded as a 'Cooling Curve' as shown in Figure 4.10(a). The magnetic moments show a decreasing trend with a lowering in temperature, due to growth of spin-spin correlation length at all stops in absence

of any external perturbation. After the lowest temperature, 2K, is reached, the system is re-warmed to room temperature without any intermittence halt and recorded magnetization is marked as a 'Warming Curve'. A reference curve is also measured following the FC protocol without any halting process. The warming curve can memorize its past thermal records and a distinct signature of previous thermal history is seen at each halting temperature. For further validation, the differentiation of the warming curve is considered as shown in Figure 4.10(b), which shows four prominent temperature peaks at the considered halting temperatures.
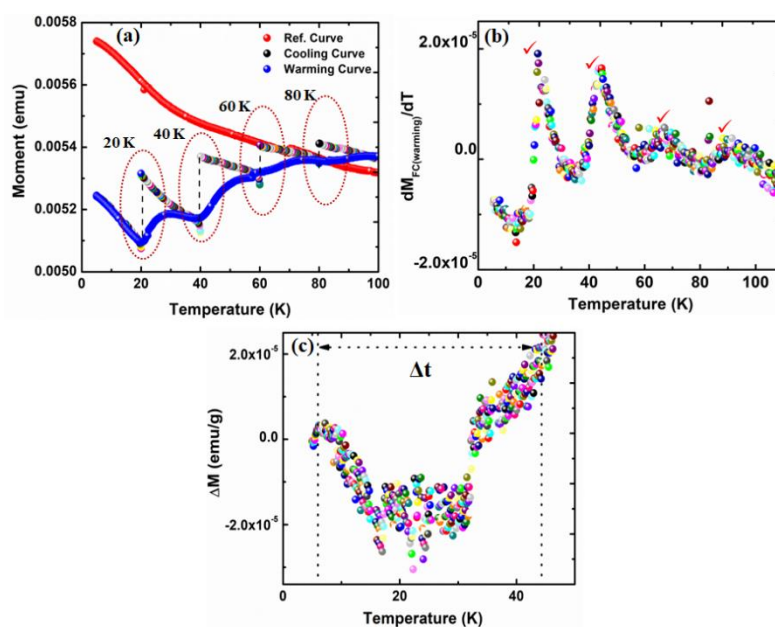

Figure 4.10: (a) Field Cooling (FC) magnetic memory effect at 20 K, 40 K, 60 K, and 80 K, (b) Differentiation of FC magnetic memory effects, (c) Zero Field Cooling (ZFC) magnetic memory effect, ΔM plot, at 40 K (as shown with an arrow) of α-MnO$_2$@NiFe$_2$O$_4$. The elliptical shapes indicate the halted temperature region in Figure (a). The right tick represents the existence of the memory effect.

In ZFC protocol, system is placed for cooling from 300K to a certain desired temperature far below the freezing temperature at a constant cooling rate [40, 41, 36]. Herein the system is kept to dwell at 30 K for 1 h. After dwelling for 1 h, system is cooled further to 2 K and warming is started without any intermittence

stopping in 100 Oe field. For reference curve, magnetization is recorded using the ZFC protocol without any halt. The difference of moments of reference curve and halt memory curve ($\Delta M = M_{ZFC}^{mem} - M_{ZFC}^{ref}$) is considered. A significant dip is observed for the range of approximately 7 K to 43 K where cooling is broken up as shown in Figure 4.10(c). This behaviour says the thermal memory history and below irreversible temperature the system is in metastable state. Thus, system shows both FC and ZFC magnetic memory effects, which is the result of interacting superparamagnetic state.

4.4.5.2 Ageing

The ageing relaxation is executed using the ZFC protocol [36] in negative temperature condition as shown in Figure 4.11(a) and Figure 4.11(b). The cooling has taken place till 30 K in no field. The ageing is allowed for 5000 seconds at a temperature of 30K and an amount of 50 Oe applied field is imposed to record the magnetization. However, initially, an exponential decay is observed, but later a broken symmetry is evident in DAN. In the next step, the temperature is reduced to a lower value such as 20 K and magnetization is measured for a duration of 7500 seconds in a 50 Oe applied field. After 7500 seconds, the system is warmed to 30 K and again measured magnetization for 7500 seconds. An asymmetric nature is seen in the continuation curve as shown in Figure 4.11(b) as the system is unable to restore its previous imprint of spin configuration. In addition, ZFC reverses relaxation ageing measurement [36] for DAN is performed as per the aforementioned protocol as shown in Figure 4.11(c) and Figure 4.11(d). The asymmetric behaviour is confirmed in the continuation curve as shown in Figure 4.11(d), which ensures the absence of memory behaviour. However, in FC condition, DAN is brought to 30 K in 50 Oe and an exponential decay of magnetic moment is observed with some broken ergodicity for 5000 seconds by turning off the field as shown in Figure 4.11(e) and Figure 4.11(f).
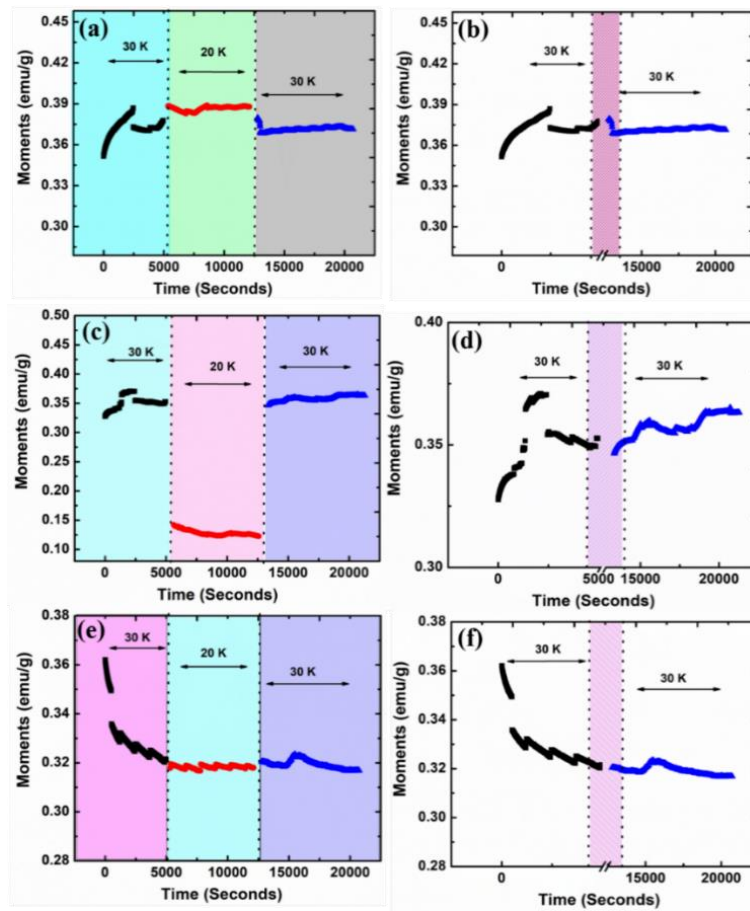
Figure 4.11: (a) Negative T-cycle ZFC ageing, (b) Continuation before and after ageing, (c) Reverse ageing relaxation in ZFC condition, (d) Continuation before and after ageing, (e) Negative FC ageing and (f) Continuation before and after ageing of α-MnO$_2$@NiFe$_2$O$_4$.

The observed non-existence of ageing behaviour ensures the absence of non-ergodic states such as spin-glass states [36], which is supported by temperature-dependent magnetization trend and ac susceptibility study. However, the observed FC magnetic memory effect below blocking temperature and ZFC magnetic memory effect with prominent Δt dip in ΔM domain are the imprint of the super-spin blocked state of the considered interacting superparamagnetic system. A broad distribution of energy barrier is ensured with an activation energy of $\frac{E_a}{k_B}$ ~ 6.6 T$_0$. Hence, modulation in dynamic magnetic behaviour is reflected in the dis-assemble interacting superparamagnetic nanosystem with a

broadening in an energy barrier, competing magnetic anisotropy, and prominent FC and ZFC memory effects.

4.5 CONCLUDING REMARKS

In conclusion, organised analysis of structural correlation and magnetic responses with non-ergodic quantum phenomena is demonstrated in a dis-assemble framework of anisotropic nanorods of the α-phase of Manganese dioxide nanorods decorated with nanoparticles of nickel ferrite, α-$MnO_2@NiFe_2O_4$. The ground state ferromagnetic behaviour is reflected in the constituent structure. The possible existence of interacting domains is evident from temperature-dependent magnetization behaviour having low temperature blocking temperature. The increasing pattern of moments below blocking temperature is a signature of non-existence of any SG states. A distinct exchange field with significant magneto-crystalline anisotropy is reflected in the considered interacting domains. The dominance of interacting superparamagnetic state is confirmed by the VF model and critical slow-down power law. The dynamic magnetic responses all together conclude the dominance of superspin blocking rather than freezing spins. The presence of interacting superparamagnetic state leads to prominent FC magnetic memory effect and ZFC magnetic memory effect, but asymmetric trend in ageing relaxation. Accordingly, the observed findings suggest that the interacting superparamagnetic state-dominated dis-assemble system with significant exchange field and magneto-crystalline anisotropy gives rise to prominent FC and ZFC memory effects with no ageing phenomena.

However, a comparison in magnetic responses in the two-dimensional ensemble of δ-$MnO_2@NiFe_2O_4$ as discussed in the previous Chapter and the disintegrated α-$MnO_2@NiFe_2O_4$ can be drawn. A competing framework of both dipolar interaction with exchange interaction in δ-$MnO_2@NiFe_2O_4$ induces the evolution of complex anisotropy framework. Such a complex framework triggers the

evolution of frustrated magnetic states. Both systems show ferromagnetic at ground state magnetization with robust bonding between δ-MnO_2 nanoflakes and $NiFe_2O_4$ nanoparticles. With sufficiently prominent magnetic memory effects in both the frameworks, the ageing relaxation trend is absent in the framework of the superparamagnetic framework of disintegrated α-MnO_2@$NiFe_2O_4$. In contrast, in the framework of cluster spin-glass state of δ-MnO_2@$NiFe_2O_4$, the evolution of hierarchical metastable states is evident and the quantum fluctuations are solely the reason behind such energy valley, that was required for glassy state transition. The observed combined effect of exchange interaction and dipolar interaction in the tightly packed frustrated low-dimensional magnets exhibit a lowering in degree of freedom, which also affects the magnetic memory effects and ageing effects. In contrast to α-MnO_2@$NiFe_2O_4$, a large number of metastable states exist despite their ground energy states. The configurational entropy in these states ranges from extensive to sub-extensive based on how the local minima are organized. The existence of spin frustration with some interfacial disordered spins disrupts the long-range order, ensuring spin-glass region. Therefore, δ-MnO_2@$NiFe_2O_4$ exhibits a magnetically frustrated state with excellent spin-dynamics behaviour. The remarkable collective behaviour of δ-MnO_2@$NiFe_2O_4$ sets off the development of a hierarchical cluster glass system that exhibits notable Field Cooling magnetic memory effects, a deeper valley of Zero Field Cooling memory effect, and negative temperature cycle ageing relaxation memory effects, which can enable novel thermal memory cell device fabrication with promising thermally storable memory in future.

References:

[1] Djurberg, C., Svedlindh, P., Nordblad, P., Hansen, M. F., Boedker, F. and Moerup, S. Dynamics of an Interacting Particle System: Evidence of Critical Slowing Down. *Physical Review Letters,* 79:5154, 1997.

[2] Bodker, F., Mørup, S., Linderoth, S. Surface effects in metallic iron nanoparticles. *Physical Review Letters,* 72:282, 1994.

[3] Deng, H., Li, X., Peng, Q., Wang, X., Chen, J., Li, Y. Monodisperse magnetic single-crystal ferrite microspheres. *Angewandte Chemie International Edition*, 44:2782, 2005.

[4] Yosida, K. Magnetic Properties of Cu-Mn Alloys. *Physical Review Letters*, 106:893, 1957.

[5] Wohlfarth, E. P. Relations between Different Modes of Acquisition of the Remanent Magnetization of Ferromagnetic Particles. Journal of Applied Physics, 29:595, 1958.

[6] Bhattacharya, K., V. Dupuis, V., Roy, D. Le and Deb, P. Progressive freezing of interacting spins in isolated finite magnetic ensembles. *Journal of Physics: Condensed Matter,* 29:045002, 2017.

[7] Saikia, K., Sarma, D. D. and P. Deb, Organization dependent collective magnetic properties of secondary nanostructures with differential spatial ordering and magnetic easy axis orientation. *Journal of Magnetism and Magnetic Materials,* 408:127, 2016.

[8] Iglesias O. and Labarta, A. Magnetic relaxation in terms of microscopic energy barriers in a model of dipolar interacting nanoparticles. *Physical Review B,* 70:144401, 2004.

[9] Felner, I. and Nowik, I. Crystal structure magnetic properties and hyperfine interactions in RFe_4Al_8 (R = rare earth) systems. *Journal of Physics and Chemistry of Solids,* 39:951, 1978.

[10] Rajendran, M., Pullar, R. C., Bhattacharya, A. K., Das, D., Chintalapudi, S. N. and Majumdar, C. K. Magnetic properties of nanocrystalline $CoFe_2O_4$ powders

prepared at room temperature: variation with crystallite size. *Journal of Magnetism and Magnetic Materials,* 232:71, 2001.

[11] Helena Gavilán, Posth, O., Bogart, L. K., Steinhoff, U., Gutiérrez, L. and Gutiérrez, M. P. How shape and internal structure affect the magnetic properties of anisometric magnetite nanoparticles. *Acta Materialia,* 125: 416, 2017.

[12] Wang, H., Mararenko, A., Cao, G., Gai, Z., Hong, K., Banerjee, P., and Zhou, S. Multifunctional 1D Magnetic and Fluorescent Nanoparticle Chains for Enhanced MRI, fluorescent Cell Imageing, And Combined Photothermal/Chemotherapy. *ACS Applied Material Interfaces,* 6(17):15309, 2014.

[13] Toulemon, D., Rastei, M. V., Schmool, D., Garitaonandia, J. S., Lezama, L., Cattoën, X., Bégin-Colin, S., and Pichon, B. P. Enhanced Collective Magnetic Properties Induced by the Controlled Assembly of Iron Oxide Nanoparticles in Chains. *Advanced Functional Materials*, 26:2454, 2016.

[14] Wilson, R. J., Hu, W., Fu, C. W. P., Koh, A. L., Gaster, R. S., Earhart, C. M., Fu, A., Heilshorn, S. C., Sinclair, R., and Wang, S. X. Formation and properties of magnetic chains for 100 nm nanoparticles used in separations of molecules and cells. *Journal of Magnetism and Magnetic Materials,* 321(10):1452, 2009.

[15] Sasaki, M., Jonsson, P. E., Takayama, H. and Mamiya, H. Ageing and memory effects in superparamagnets and superspin glasses. *Physical Review B,* 71: 104405, 2005.

[16] Samarakoon, A., Sato, T. J., Chen, T., Chern, G.-W., Yang, J., Klich, I, Sinclair, Zhou, R. H. and Lee, S.-H. Ageing, memory, and nonhierarchical energy landscape of spin jam, *Proceedings of the National Academy of Sciences,* 114: 11806, 2016.

[17] Xiang, B., Ling, D., Lou, H. and Gu, H. 3D hierarchical flower-like nickel ferrite/manganese dioxide toward lead (II) removal from aqueous water. *Journal of hazardous materials,* 325:178, 2017.

[18] Gebauer, R., Gerstmann, U., Gougoussis, C., Kokalj, A., Lazzeri, M., Martin-Samos, L., Marzari, N., Mauri, F., Mazzarello, R., Paolini, S., Pasquarello, A., Paulatto, L., Sbraccia, C., Scandolo, S., Sclauzero, G., Seitsonen, A. P., Smogunov, A., Umari, P., and Wentzcovitch, R. M. QUANTUM ESPRESSO: a modular and open-source software project for quantum simulations of materials. *Journal of Physics: Condensed Matter*, 21(39):395502, 2009.

[19] Rappe, A. M., Rabe, K. M., Kaxiras, E. and Joannopoulos, J. D. Optimized pseudopotentials. *Physical Review B,* 44:13175, 1991.

[20] Perdew, J. P. and Zunger, A. Self-interaction correction to density-functional approximations for many-electron systems. *Physical Review B,* 23:5048, 1981.

[21] Nayek, C., Samanta, S., Manna, K., Pokle, A., Nanda, B. R. K., Anil Kumar, P. S. and Murugavel, P. Spin-glass state in nanoparticulate $(La_{0.7}Sr_{0.3}MnO_3)_{1-x}$ $(BaTiO_3)_x$ solid solutions: Experimental and density-functional studies. *Physical Review B,* 93:094401, 2016.

[22] Monkhorst H. J. and Pack, J. D. Special points for Brillouin-zone integrations. *Physical Review B,* 13:5188, 1976.

[23] Zhang, R., Yu, X., nam, K.-W., Ling, C., Arthur, T. S., Song, W., Knapp, A. M., Ehrlich, S. N., Yang, X.-Q. and Matsui, M. α-MnO_2 as a cathode material for rechargeable Mg batteries. *Electrochemistry Communications,* 23:110, 2012.

[24] Feng, S., Yang, W. and Zhongbing, W. Synthesis of porous $NiFe_2O_4$ microparticles and its catalytic properties for methane combustion, *Materials Science and Engineering: B,* 176:1509, 2011.

[25] Kohlbrecher, J. SASfit: A program for fitting simple structural models to small angle scattering data, 2023.

[26] Saikia, K., Kaushik, S.D., Sen, D., Mazumder, S. and Deb. P. Fatty acid as structure directing agent for controlled secondary growth of CoFe2O4 nanoparticles to achieve mesoscale assemblies: A facile approach for developing hierarchical structures, *Applied Surface Science,* 379:530, 2016.

[27] Perron, H., Mellier, T., Domain, C., Roques, J., Simoni, E., Drot, R. and Catalette, H. Structural investigation and electronic properties of the nickel ferrite $NiFe_2O_4$: a periodic density functional theory approach. *Journal of Physics: Condensed Matter,* 19:346219, 2007.

[28] Zuo, X., Yan, S., Barbiellini, B., Harris, V. G. and Vittoria, C. A Computational Study of Nickel Ferrite, *Journal of Magnetism and Magnetic Materials.* 303:e432, 2006.

[29] Saikia, K., Kaushik, S.D., Sen, D., Mazumder, S. and Deb. P. Fatty acid as structure directing agent for controlled secondary growth of $CoFe_2O_4$ nanoparticles to achieve mesoscale assemblies: A facile approach for developing hierarchical structures. *Applied Surface Science*, 379:530, 2016.

[30] Bhattacharya, K., V. Dupuis, V., Roy, D. Le and Deb, P. Progressive freezing of interacting spins in isolated finite magnetic ensembles. *Journal of Physics: Condensed Matter,* 29:045002, 2017.

[31] Devi, E. C. and Soibam, I. Law of Approach to Saturation in Mn–Zn Ferrite Nanoparticles, *Journal of Superconductivity and Novel Magnetism.* 32:1293, 2019.

[32] Chudnovsky, E. M., Saslow, W. M. and Serota, R. A. Ordering in ferromagnets with random anisotropy. *Physical Review B,* 33:251, 1986.

[33] Aharony A. and Pytte, E. Infinite Susceptibility Phase in Random Uniaxial Anisotropy Magnets. *Physical Review Letters,* 45:1583, 1980.

[34] Yadav, K., Sharma, M., Singh, S. and Mukherjee, K. Exotic magnetic behaviour and evidence of cluster glass and Griffiths like phase in Heusler alloys $Fe_{2-x}Mn_xCrAl$ ($0 \leq x \leq 1$). *Scientific Reports,* 9:15888, 2019.

[35] Ghanta, S., Das, A., Jana, P., Vrtnik, S., Gačnik, D., Luzar, J., Jelen, A., Koželj, P., Wencka, M., Dolinšek, J. Structure and Spin-Glass Magnetism of the $Mn_xNi_2 Zn_{11-x}$ Pseudobinary γ-Brasses at Low Mn Contents. *Inorganic Chemistry,* 60:12226, 2021.

[36] Bag, P., Baral, P. R. and Nath, R. Cluster spin-glass behavior and memory effect in $Cr_{0.5}Fe_{0.5}Ga$, *Physical Review B,* 98:144436, 2018.

[37] Nadeem, K., Krenn, H., Traussing, T. and Letofsky-Papst, I. Distinguishing magnetic blocking and surface spin-glass freezing in nickel ferrite nanoparticles. *Journal of Applied Physics,* 109:013912, 2011.

[38] Gupta, S., Sathe, V. G., Suresh, K. G. and Siruguri, V. Evidence for cluster spin-glass like phase with longitudinal conical magnetic structure in Ga doped M-type barium hexaferrite, $BaFe_{10}Ga_2O_{19}$. *Journal of Magnetism and Magnetic Materials,* 540:168483, 2021.

[39] Bag, P., Somesh, K. and Nath, R. A study of cluster spin-glass behaviour at the critical composition $Mn_{0.73}Fe_{0.27}NiGe$. *Journal of Magnetism and Magnetic Materials,* 497:165977, 2020.

[40] Chakrabarty, T., Mahajan, A. V. and Kundu, S. Cluster spin glass behavior in geometrically frustrated $Zn_3V_3O_8$. *Journal of Physics: Condensed Matter,* 26: 405601, 2014.

[41] Banerjee, S., Panda, D. P., Yanda, P. and Sundaresan, A. Canonical spin glass and cluster glass behavior in the polymorphs of $LiFeSnO_4$. *Physical Review Materials,* 7:034405, 2023.